

The extended Fourier pseudospectral time-domain method for atmospheric sound propagation

[Maarten Hornikx](#) and [VEORoger Waxler](#) and [VEOJens Forssén](#) and [VEO](#)

Citation: [The Journal of the Acoustical Society of America](#) **128**, 1632 (2010); doi: 10.1121/1.3474234

View online: <http://dx.doi.org/10.1121/1.3474234>

View Table of Contents: <http://asa.scitation.org/toc/jas/128/4>

Published by the [Acoustical Society of America](#)

The extended Fourier pseudospectral time-domain method for atmospheric sound propagation

Maarten Hornikx^{a)}

Department of Civil and Environmental Engineering, Division of Applied Acoustics, Chalmers University of Technology, SE-41296 Göteborg, Sweden

Roger Waxler

National Center for Physical Acoustics, University of Mississippi, 1 Coliseum Drive, Mississippi 38677

Jens Forssén

Department of Civil and Environmental Engineering, Division of Applied Acoustics, Chalmers University of Technology, SE-41296 Göteborg, Sweden

(Received 10 December 2009; revised 2 July 2010; accepted 12 July 2010)

An extended Fourier pseudospectral time-domain (PSTD) method is presented to model atmospheric sound propagation by solving the linearized Euler equations. In this method, evaluation of spatial derivatives is based on an eigenfunction expansion. Evaluation on a spatial grid requires only two spatial points per wavelength. Time iteration is done using a low-storage optimized six-stage Runge-Kutta method. This method is applied to two-dimensional non-moving media models, one with screens and one for an urban canyon, with generally high accuracy in both amplitude and phase. For a moving atmosphere, accurate results have been obtained in models with both a uniform and a logarithmic wind velocity profile over a rigid ground surface and in the presence of a screen. The method has also been validated for three-dimensional sound propagation over a screen. For that application, the developed method is in the order of 100 times faster than the second-order-accurate FDTD solution to the linearized Euler equations. The method is found to be well suited for atmospheric sound propagation simulations where effects of complex meteorology and straight rigid boundary surfaces are to be investigated.

© 2010 Acoustical Society of America. [DOI: 10.1121/1.3474234]

PACS number(s): 43.28.Js, 43.20.El, 43.28.Fp, 43.28.En [VEO]

Pages: 1632–1646

I. INTRODUCTION

Modeling atmospheric sound propagation for linear acoustic problems often requires that one accurately includes effects of the ground surface, meteorological effects such as refraction and scattering and effects due to obstacles of natural (e.g., hills) and man-made (e.g., houses) nature. Many methods are limited in application due to approximations inherent to the method.

Ray based methods, such as the engineering models designed for use in the field of community noise control; see e.g., Refs. 1 and 2; can be used to model diverse atmospheric and ground conditions and can handle complex topography but are not suitable for problems which depend fundamentally on wavelength such as penetration into the acoustic shadow zones caused by urban courtyards or atmospheric upward refraction. Full wave methods, such as the fast field program (FFP) and the parabolic equation (PE) method, have been developed for more general meteorological conditions; see e.g., Ref. 3 for references; but have difficulties with obstacles and complex topography. To model propagation in arbitrary geometries, the boundary element method (BEM)

has been used but has difficulties in handling complex meteorology and has been mainly restricted to the simple meteorological conditions of linear, range-independent sound speed profiles; see e.g., Ref. 4.

In this paper, numerical solutions to the following linearized Euler equations are sought,

$$\begin{aligned}\frac{\partial \mathbf{u}}{\partial t} &= -(\mathbf{u}_0 \cdot \nabla) \mathbf{u} - (\mathbf{u} \cdot \nabla) \mathbf{u}_0 - \frac{1}{\rho_0} \nabla p, \\ \frac{\partial p}{\partial t} &= -\mathbf{u}_0 \cdot \nabla p - \rho_0 c^2 \nabla \cdot \mathbf{u} - s \delta(\mathbf{x}|\mathbf{x}_s),\end{aligned}\quad (1)$$

with c the adiabatic speed of sound, ρ_0 the mean density, \mathbf{u}_0 the wind velocity vector, \mathbf{u} and p the acoustic velocity and pressure, respectively, $\delta(\mathbf{x}|\mathbf{x}_s)$ the Dirac delta function and $s(t)$ the source strength. We will denote the components of the velocity by $\mathbf{u}=[u,v,w]^T$. The principle of solution is based on treating (1) as a system of first order equations in t . One evaluates the spatial differential operator using some numerical method and then solves the first order system using, for example, a Runge-Kutta scheme.

In the past decade, finite-difference time-domain (FDTD) solutions to the linearized Euler equations have been developed which can accurately model sound propagation under complex meteorological and ground conditions

^{a)}Author to whom correspondence should be addressed. Present address: Department of Mechanical Engineering, Noise and Vibration Engineering Group, K. U. Leuven Celestijnenlaan 300b-bus 2420, 3001 Heverlee, Belgium. Electronic mail: maarten.hornikx@mech.kuleuven.be

and through complex geometries.⁵⁻⁷ Applications to sound propagation over an impedance ground surface, to sound propagation over a screen in a turbulent atmosphere,⁸ to a shielded urban environment^{9,10} and to an urban environment modeled in two dimensions, i.e., a horizontal propagation domain,¹¹ have been developed. In these methods, the spatial derivatives arising in the linearized Euler equations are approximated by finite-difference relations, typically second-order-accurate requiring 10 spatial points per wavelength for accurate results. The main limitation of the FDTD methods is therefore their computational burden. Variations, such as the transmission line model,¹²⁻¹⁴ and dispersion-relation-preserving (DRP) schemes^{15,16} require a similar computational effort.

A way to solve the linearized Euler equations with lower computational costs is to make use of a pseudospectral time-domain (PSTD) method. The most common PSTD methods are the Fourier and the Chebyshev methods. The Fourier pseudospectral methods are based on estimating spatial derivatives using Fourier transforms. Explicitly,

$$\frac{\partial}{\partial x} \begin{bmatrix} u(x,y,z,t) \\ v(x,y,z,t) \\ w(x,y,z,t) \\ p(x,y,z,t) \end{bmatrix} = \frac{1}{2\pi} \int_{-\infty}^{\infty} \int_{-\infty}^{\infty} j k e^{jk(x-x')} \times \begin{bmatrix} u(x',y,z,t) \\ v(x',y,z,t) \\ w(x',y,z,t) \\ p(x',y,z,t) \end{bmatrix} dx' dk, \quad (2)$$

and similarly for y and z -derivatives. Such Fourier transform based methods work well for propagation in a single unbounded fluid with small and slowly varying inhomogeneities and have been applied to solve a model wave equation for sound propagation through biological tissue.¹⁷ This approach can produce very efficient algorithms, as compared to finite difference schemes, since coarser spatial grids, two points per wavelength, are allowed for and since the calculations can be done using the Fast Fourier Transform (FFT) algorithm. The Fourier PSTD method makes use of the whole grid solution to calculate spatial derivatives and can be shown to be equivalent to a finite-difference relation with an infinite order of accuracy.¹⁸ Errors are introduced by non-resolved wave numbers.

For many applications, the PSTD method has been shown to be computationally faster and to require less memory storage than the FDTD method^{19,20} and has widely been used in fields such as seismic wave propagation, fluid dynamics and electromagnetics. Pseudospectral methods are receiving increased attention in the acoustical community with applications in aeroacoustics²⁰ and bioacoustics.^{17,21} However, few applications of the PSTD method to atmospheric sound propagation have appeared.²²⁻²⁴

Fourier methods are problematic in the presence of boundaries since these introduce discontinuities which are poorly resolved by Fourier transforms. The Chebyshev PSTD method may be used to solve problems in bounded media and media with interfaces. In the Chebyshev PSTD method, however, a particular non-uniform grid is required so that in practice the domain needs to be divided in subdomains and more spatial points per wavelength than in the Fourier PSTD are necessary. Further, the method is more sensitive to instability; see e.g., Ref. 18. Recently, an extended Fourier PSTD method has been presented to model fluids with discontinuous properties in 1D²⁵ and 2D,²⁶ and the accuracy of this method for simple geometrical cases was thoroughly studied. The method relies on an eigenfunction expansion to compute spatial derivatives. These eigenfunction expansions can be expressed as linear combinations of Fourier transforms, so that the resulting algorithms share the efficiency of the Fourier methods. For example, for propagation over a rigid ground surface the form

$$\frac{\partial}{\partial z} \begin{bmatrix} u(x,y,z,t) \\ v(x,y,z,t) \\ w(x,y,z,t) \\ p(x,y,z,t) \end{bmatrix} = \frac{2}{\pi} \int_0^{\infty} \int_0^{\infty} \times \begin{bmatrix} k \cos(kz) \cos(kz') u(x,y,z',t) \\ k \cos(kz) \cos(kz') v(x,y,z',t) \\ -k \sin(kz) \sin(kz') w(x,y,z',t) \\ k \cos(kz) \cos(kz') p(x,y,z',t) \end{bmatrix} dz' dk, \quad (3)$$

may be used for derivatives with respect to z . In this form, pressure and horizontal components of the velocity are expressed as cosine transforms while the vertical component of the velocity is expressed as a sine transform.

In this paper, the approach developed in Ref. 26 for the wave equation in media with material discontinuities is extended to the system (1) in order to present a highly accurate and computationally efficient time-domain method to model propagation in moving inhomogeneous media with planar interfaces. Propagation over rigid ground surfaces, around rectangular obstacles, and in media with discontinuous density is considered. Possible applications are to atmospheric infrasound propagation, to propagation over a noise barrier in the presence of complex three-dimensional (3-D) meteorological effects, and to propagation through urban environments and sound propagation over urban areas including meteorology. In Sec. II, the details of the method are reported, focusing on the evaluation of the spatial derivatives, the time derivative operator, the source function and the treatment of open boundaries. The method is then validated in Sec. III for simple yet typical atmospheric sound propagation geometries such as a thin and thick screen, a double screen and an urban canyon. For the canyon case, both rigid and finite impedance

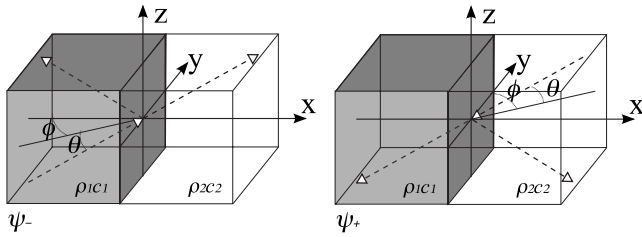


FIG. 1. The 3-D problem of two semi-infinite fluid media, medium 1 and medium 2, with the interface at $(0, y, z)$ and $c_1 \leq c_2$. Directions of eigenfunctions ψ_- and ψ_+ are shown according to Eq. (10). In this paper, different media are considered to have the same sound speed, i.e., $c_1 = c_2$.

boundaries are considered. Further validations are made for atmospheric acoustic problems with specific wind velocity profiles. Finally, the application of the method in three dimensions is demonstrated by a calculation of sound propagation over a screen in neutral and downwind meteorological conditions.

II. DETAILS OF THE EXTENDED FOURIER PSTD METHOD

A. Spatial derivative operator: Extended Fourier PS method

We first consider the general problem of two semi-infinite fluid media with piecewise homogeneous properties $(\rho_1, c_1$ and $\rho_2, c_2)$; see Fig. 1. We will later drop the inequality of the sound speeds of both media and consider different densities only. The method used to calculate the spatial derivatives for the two-media problem is based on the homogeneous non-moving linearized Euler equations.

Introduce the operators

$$L = \begin{bmatrix} 0 & 0 & 0 & j\partial_x \\ 0 & 0 & 0 & j\partial_y \\ 0 & 0 & 0 & j\partial_z \\ j\partial_x & j\partial_y & j\partial_z & 0 \end{bmatrix}, \quad (4)$$

$$R_j = \begin{bmatrix} \rho_j & 0 & 0 & 0 \\ 0 & \rho_j & 0 & 0 \\ 0 & 0 & \rho_j & 0 \\ 0 & 0 & 0 & \frac{1}{\rho_j c_j^2} \end{bmatrix}, \quad (5)$$

and

$$V = \begin{bmatrix} \partial_x u_0 + (\nabla \cdot) u_0 & \partial_y u_0 & \partial_z u_0 & 0 \\ \partial_x v_0 & \partial_y v_0 + (\nabla \cdot) u_0 & \partial_z v_0 & 0 \\ \partial_x w_0 & \partial_y w_0 & \partial_z w_0 + (\nabla \cdot) u_0 & 0 \\ 0 & 0 & 0 & (\nabla \cdot) u_0 \end{bmatrix}, \quad (6)$$

with $\partial_n = \partial / \partial n$ and with the notation $(\nabla \cdot) u_0 f = \nabla \cdot (u_0 f)$, and introduce the solution vector

$$q(x, t) = \begin{bmatrix} u(x, t) \\ v(x, t) \\ w(x, t) \\ p(x, t) \end{bmatrix}. \quad (7)$$

Assuming the mean flow to be incompressible, $\nabla \cdot u_0 = 0$, Eq. (1) can be written

$$\frac{\partial q}{\partial t} = [jR_j^{-1}L - V]q - s(t)\delta(x|x_s), \quad (8)$$

with $s = [0, 0, 0, s]^T$ the source vector and where the subscript j denotes the medium. Note that L is a self-adjoint operator and R_j a matrix with medium dependent constants. The spatial derivatives in Eq. (8) will be calculated using the eigenfunction expansion for L . The following eigenvalue problem is now solved:²⁷

$$[L - \epsilon R_j]\psi(\epsilon, \phi, \theta, x) = 0. \quad (9)$$

Here ϵ are the eigenvalues and $\psi(\epsilon, \phi, \theta, x)$ the orthogonal eigenfunctions. The four eigenvalues, found from $\det(L - \epsilon R_j) = 0$, are $\epsilon = 0, 0, -k_j c_j, k_j c_j$. These eigenvalues correspond to two time independent components, which are uninteresting, and two propagating waves in time with $k_j \in [0, \infty)$, which constitute the solutions of interest for, respectively, the $e^{-j\omega t}$ and $e^{j\omega t}$ convention. Since the domain of interest is unbounded, there is a continuum of eigenvalues. The eigenfunctions can be seen as a set of plane wave solutions with different angles of incidence, depicted in Fig. 1. To facilitate the use of Fast Fourier Transforms, the eigenfunctions are written as a function of the wave number vector $k_1 = [k_{x1}, k_y, k_z]$. The mutually orthogonal generalized eigenfunctions that are solutions to Eq. (9) for $\epsilon = k_j c_j$ are:

$$\psi_-(k_1, x) = N_-(k_1) \cdot \begin{cases} \begin{bmatrix} \frac{k_{x1}}{k_1 \rho_1 c_1} (\alpha_1 e^{-jk_1 x} - \beta_1 e^{-j\bar{k}_1 x}) \\ \frac{k_y}{k_1 \rho_1 c_1} (\alpha_1 e^{-jk_1 x} + \beta_1 e^{-j\bar{k}_1 x}) \\ \frac{k_z}{k_1 \rho_1 c_1} (\alpha_1 e^{-jk_1 x} + \beta_1 e^{-j\bar{k}_1 x}) \\ \alpha_1 e^{-jk_1 x} + \beta_1 e^{-j\bar{k}_1 x} \end{bmatrix}, & x \leq 0, \\ \begin{bmatrix} \frac{k_{x2}}{k_2 \rho_2 c_2} e^{-jk_2 x} \\ \frac{k_y}{k_2 \rho_2 c_2} e^{-jk_2 x} \\ \frac{k_z}{k_2 \rho_2 c_2} e^{-jk_2 x} \\ e^{-jk_2 x} \end{bmatrix}, & x \geq 0, \end{cases}$$

$$\psi_{\pm}(\mathbf{k}_1, \mathbf{x}) = N_{\pm}(\mathbf{k}_1) \cdot \begin{cases} \begin{bmatrix} \frac{-k_{x1}}{k_1 \rho_1 c_1} e^{ik_1 x} \\ \frac{-k_y}{k_1 \rho_1 c_1} e^{ik_1 x} \\ \frac{-k_z}{k_1 \rho_1 c_1} e^{ik_1 x} \\ e^{ik_1 x} \end{bmatrix}, & x \leq 0, \\ \begin{bmatrix} \frac{-k_{x1}}{k_2 \rho_2 c_2} (\alpha_2 e^{ik_2 x} - \beta_2 e^{i\bar{k}_2 x}) \\ \frac{-k_y}{k_2 \rho_2 c_2} (\alpha_2 e^{ik_2 x} + \beta_2 e^{i\bar{k}_2 x}) \\ \frac{-k_z}{k_2 \rho_2 c_2} (\alpha_2 e^{ik_2 x} + \beta_2 e^{i\bar{k}_2 x}) \\ \alpha_2 e^{ik_2 x} + \beta_2 e^{i\bar{k}_2 x} \end{bmatrix}, & x \geq 0, \end{cases} \quad (10)$$

with $\mathbf{k}_1 \cdot \mathbf{x} = k_{x1}x + k_y y + k_z z$, $\bar{\mathbf{k}}_1 \cdot \mathbf{x} = -k_{x1}x + k_y y + k_z z$, $k_1 = |\mathbf{k}_1|$, $k_{x1} \in [0, \infty)$ and $k_y, k_z \in (-\infty, \infty)$. The coefficients $\alpha_1, \alpha_2, \beta_1, \beta_2$ can be found by the physical interface conditions at $x=0$ and $N_{\pm}(\mathbf{k}_1)$ are normalization coefficients, determined by the condition of completeness:

$$\delta(\mathbf{x}_1 - \mathbf{x}_2) \begin{bmatrix} 1 & 0 & 0 & 0 \\ 0 & 1 & 0 & 0 \\ 0 & 0 & 1 & 0 \\ 0 & 0 & 0 & 1 \end{bmatrix} = \sum_{\pm} \int_{-\infty}^{\infty} \int_{-\infty}^{\infty} \int_0^{\infty} \times \psi_{\pm}(\mathbf{k}_1, \mathbf{x}_1) \overline{\psi_{\pm}(\mathbf{k}_1, \mathbf{x}_2)}^T R_j d\mathbf{k}_1, \quad (11)$$

where the overbar denotes the complex conjugate. We can now decompose the variable vector $\mathbf{q}(\mathbf{x}, t)$, the solution of Eq. (8) at a certain time, into the orthogonal eigenfunctions $\psi_{\pm}(\mathbf{k}_1, \mathbf{x})$ by writing

$$\mathbf{Q}_{\pm}(\mathbf{k}_1, t) = \int_{-\infty}^{\infty} \int_{-\infty}^{\infty} \int_0^{\infty} \mathbf{q}(\mathbf{x}, t) \overline{\psi_{\pm}(\mathbf{k}_1, \mathbf{x})}^T R_j d\mathbf{x}, \quad (12)$$

with $\mathbf{Q}_{\pm}(\mathbf{k}, t)$ the wave number variables and where

$$\mathbf{q}(\mathbf{x}, t) = \sum_{\pm} \int_{-\infty}^{\infty} \int_{-\infty}^{\infty} \int_0^{\infty} \mathbf{Q}_{\pm}(\mathbf{k}_1, t) \psi_{\pm}(\mathbf{k}_1, \mathbf{x}) d\mathbf{k}_1. \quad (13)$$

The action of the spatial derivative operator $L\mathbf{q}(\mathbf{x}, t)$ may be computed using the eigenvalue equation Eq. (9) and the eigenfunction expansion (13):

$$L\mathbf{q}(\mathbf{x}, t) = \sum_{\pm} \int_{-\infty}^{\infty} \int_{-\infty}^{\infty} \int_0^{\infty} \epsilon R_j \mathbf{Q}_{\pm}(\mathbf{k}_1, t) \psi_{\pm}(\mathbf{k}_1, \mathbf{x}) d\mathbf{k}_1. \quad (14)$$

The spatial derivative operator L can thus be calculated by applying a transform to $\mathbf{q}(\mathbf{x}, t)$ through the eigenfunctions over the spatial variables, multiplying the obtained wave number transforms $\mathbf{Q}_{\pm}(\mathbf{k}, t)$ by ϵR_j and inverse transforming over the wave number \mathbf{k}_1 through the eigenfunctions. Once $L\mathbf{q}$ has been computed it may be substituted in Eq. (8). Most

of the transforms in Eqs. (12) and (14) can be done by FFTs, as follows after inserting the eigenfunctions. However, as pointed out by Hornikx and Waxler for the wave equation,²⁶ modeling the problem with $c_2 \neq c_1$ using a spatial discretization in both media yields errors related to a disagreement of the maximum resolved frequencies in both media. A way to use the method for the two-fluid problem with $c_2 \neq c_1$ by only discretizing one fluid is proposed in that paper. The method is restricted to geometries with known eigenfunctions. These eigenfunctions are not available for geometries of interest in atmospheric acoustics as used in Sec. III, at least not in an analytical form. However, when $c_2 = c_1$, we obtain $\mathbf{k}_2 = \mathbf{k}_1 = \mathbf{k}$ and the coefficients $\alpha_1, \alpha_2, \beta_1, \beta_2$ and the normalization coefficients N_{\pm} become constants. In this case the evaluation of spatial partial derivatives is straightforward. The numerical approximations for the derivatives used in this paper are worked out and presented in the Appendix.

In stationary media, with $\mathbf{u}_0 = 0$, the operator V in Eq. (8) is zero. In this case, to estimate the required spatial derivatives, it suffices to evaluate the action of L using Eq. (14). In contrast, in moving media with $\mathbf{u}_0 \neq 0$, additional derivatives arise which can be evaluated using the eigenfunction expansion directly as in the Appendix. Cross-derivatives such as $\partial u / \partial z$ appear in the linearized Euler equations and introduce discontinuities which are not resolved by the eigenfunction expansion, however, in Eq. (8), with the definition Eq. (6), such cross derivatives arise only as derivatives of products of atmospheric and acoustic velocity components, such as $\partial w_0 u / \partial z$. Assuming non-slip wall conditions for the mean flow, the product of a component of the mean flow with an acoustic variable has compact support within the modeled atmosphere. Such products are therefore not discontinuous and can be differentiated using the eigenfunction expansion.

Using a Fourier PS method to calculate first-order spatial derivatives with staggered grids for pressure and velocity components was shown to be advantageous over a collocated grid.^{28,29} In this, and all that follows, a staggered uniform spatial grid will be adopted (see the Appendix). Since the evaluation of Eq. (14) involves FFTs, accuracy is determined by the Nyquist criterium: the grid spacing must be less than one half of the smallest resolved wavelength. If Δx is the grid spacing then $k_{\max} = \pi / \Delta x$ is the largest resolved wave number. Components with wavenumbers greater than k_{\max} will produce noise through aliasing and must therefore be small. High wave number components may be induced by large variations of mean density, sound speed and wind velocity. However, sound speed and density tend to be much more slowly varying than wind velocity so this is primarily a consideration in moving media.

B. Time iteration: Runge-Kutta method

Runge-Kutta methods are commonly used to solve initial value problems and compute a single discrete time step by several intermediate steps, thereby creating a higher order of accuracy than the second-order accurate finite-difference representations commonly used in FDTD implementations for atmospheric sound propagation. The coefficients in the Runge-Kutta methods can be calculated by Taylor series or

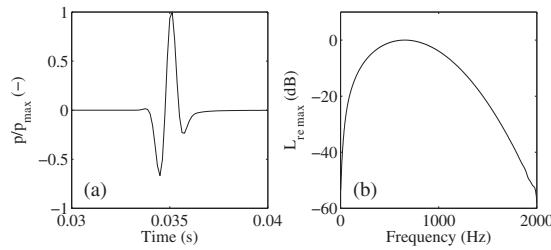


FIG. 2. Two-dimensional free field signal calculated with the extended Fourier PSTD method on an equidistant grid with the source function of Eq. (16). The maximum resolved frequency $f_{\max}=c/2\Delta x=2000$ Hz, $\Delta t=\Delta x/2c$ and source-receiver distance equal to $100 \Delta x$. (a) Time signal; (b) Frequency content of (a).

by optimization procedures to minimize dissipation and dispersion errors, e.g., Refs. 16, 30, and 31. Here, the low-storage optimized six-stage Runge-Kutta scheme by Bogey and Bailly (further RKo6s) has been used.¹⁶ This algorithm has minimized the dispersion and dissipation error for frequencies corresponding to 4 spatial points per wavelength. Explicitly, Eq. (8) is solved in time by a six-stage Runge-Kutta method which can be written as:

$$\begin{aligned} q(\mathbf{x}, t_0) &= q(\mathbf{x}, t), \\ q(\mathbf{x}, t_i) &\approx q(\mathbf{x}, t_0) - \gamma_i \Delta t (W q(\mathbf{x}, t_{i-1}) + s(t_{i-1}) \delta(\mathbf{x}|\mathbf{x}_s)), \\ \text{for } i &= 1 \dots 6, \\ q(\mathbf{x}, t + \Delta t) &\approx q(\mathbf{x}, t_6), \end{aligned} \quad (15)$$

with $W = [-jR_j^{-1}L + V]$, i the integer stage number within a Runge-Kutta time step, γ_i a real number between 0 and 1 as in Ref. 16 and Δt a discrete time step. In the numerical solution, an absorption layer is applied to the non-reflecting boundaries. This changes the time iteration procedure slightly, as described in Sec. II C. The RKo6s method only requires storage of the variables at two time levels.

Throughout, the source function

$$s(t) = A \sin(2\pi f_c t) e^{-a(t-t_c)^2}, \quad (16)$$

is used. A is the amplitude, f_c and t_c are the central frequency and time and a a constant determining the bandwidth. The drawback of this source function is that it changes the pressure value after every time step at a single point in space. This leads to a spatial discontinuity, causes a ringing effect in the time response and limits the maximum discrete time step using a pseudospectral method. Figure 2 shows a calculated 2-D free field signal with the source function given by Eq. (16). The spatial sampling is chosen such that the maximum resolved frequency $f_{\max}=c/2\Delta x=2000$ Hz (where $\Delta x=\lambda_{\min}/2$). The source function parameters used are $A=1$ N m/s, $f_c=f_s/8$ Hz, $t_c=0.01$ s, $a=3f_s^2/16$ s⁻² and $\Delta t=1/(2f_s)$ s. As no ringing effect are visible in the time response, the above variable values and $f_{\max}=2000$ Hz have been used for most calculations of this paper.

C. Reflection free boundaries

A widely adopted method to obtain a reflection free boundary at open domain ends is the perfectly matched layer

(PML), as first presented by Berenger for electromagnetics problems.³² Besides avoiding reflections, such an absorption layer will also cause the variables to have compact support in the computational domain, which is a necessity in the extended Fourier PSTD method to avoid wrap-around effects. The PML in acoustics has been used by e.g., van Renterghem,⁹ Hu³³ and Tabei *et al.*³⁴ Several types of PMLs have been presented where both the pressure and velocities are split into components,³³ only the pressure is split³² or none of the variables are split.³⁵ Also the convolutional PML offers a solution without splitting the variables.³⁶ We have here followed the approach of Berenger and split the pressure into components parallel and perpendicular to the PML. The idea is to include an absorption layer at the edge of the computational domain acting on the normal components of the velocity and pressure, which returns a layer without reflections for all incoming propagation angles. The 3-D linearized Euler equations with PML then read:

$$\begin{aligned} \frac{\partial u}{\partial t} &= -\mathbf{u} \cdot \nabla u_0 - \nabla \cdot (\mathbf{u}_0 u) - \frac{1}{\rho_0} \frac{\partial p}{\partial x} - \sigma_x(\mathbf{x})u, \\ \frac{\partial v}{\partial t} &= -\mathbf{u} \cdot \nabla v_0 - \nabla \cdot (\mathbf{u}_0 v) - \frac{1}{\rho_0} \frac{\partial p}{\partial y} - \sigma_y(\mathbf{x})v, \\ \frac{\partial w}{\partial t} &= -\mathbf{u} \cdot \nabla w_0 - \nabla \cdot (\mathbf{u}_0 w) - \frac{1}{\rho_0} \frac{\partial p}{\partial z} - \sigma_z(\mathbf{x})w, \\ \frac{\partial p_x}{\partial t} &= -\rho_0 c^2 \frac{\partial u}{\partial x} - \nabla \cdot (\mathbf{u}_0 p_x) - \frac{s(t)\delta(\mathbf{x}|\mathbf{x}_s)}{\mathcal{D}} - \sigma_x(\mathbf{x})p_x, \\ \frac{\partial p_y}{\partial t} &= -\rho_0 c^2 \frac{\partial v}{\partial y} - \nabla \cdot (\mathbf{u}_0 p_y) - \frac{s(t)\delta(\mathbf{x}|\mathbf{x}_s)}{\mathcal{D}} - \sigma_y(\mathbf{x})p_y, \\ \frac{\partial p_z}{\partial t} &= -\rho_0 c^2 \frac{\partial w}{\partial z} - \nabla \cdot (\mathbf{u}_0 p_z) - \frac{s(t)\delta(\mathbf{x}|\mathbf{x}_s)}{\mathcal{D}} - \sigma_z(\mathbf{x})p_z, \end{aligned} \quad (17)$$

with $p=p_x+p_y+p_z$ and \mathcal{D} the dimensionality of the problem. The PML coefficients $\boldsymbol{\sigma}(\mathbf{x})=[\sigma_x(\mathbf{x}), \sigma_y(\mathbf{x}), \sigma_z(\mathbf{x})]^T$ are zero or positive in the PML and zero elsewhere. For numerical stability in pseudospectral methods, we write the implementation of the PML as in Ref. 37:

$$\begin{aligned} e^{-\sigma_x t} \frac{\partial e^{\sigma_x t} u}{\partial t} &= -\mathbf{u} \cdot \nabla u_0 - \nabla \cdot (\mathbf{u}_0 u) - \frac{1}{\rho_0} \frac{\partial p}{\partial x}, \\ e^{-\sigma_y t} \frac{\partial e^{\sigma_y t} v}{\partial t} &= -\mathbf{u} \cdot \nabla v_0 - \nabla \cdot (\mathbf{u}_0 v) - \frac{1}{\rho_0} \frac{\partial p}{\partial y}, \\ e^{-\sigma_z t} \frac{\partial e^{\sigma_z t} w}{\partial t} &= -\mathbf{u} \cdot \nabla w_0 - \nabla \cdot (\mathbf{u}_0 w) - \frac{1}{\rho_0} \frac{\partial p}{\partial z}, \\ e^{-\sigma_x t} \frac{\partial e^{\sigma_x t} p_x}{\partial t} &= -\rho_0 c^2 \frac{\partial u}{\partial x} - \nabla \cdot (\mathbf{u}_0 p_x) - \frac{s(t)\delta(\mathbf{x}|\mathbf{x}_s)}{\mathcal{D}}, \end{aligned}$$

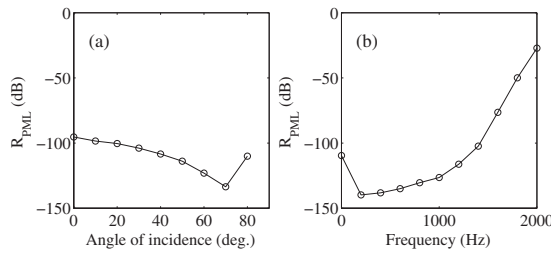


FIG. 3. Arithmetic averaged reflection coefficients of the PML in the extended Fourier PSTD method. (a) Frequency averaged results; (b) Angular averaged results. Following PML coefficients have been used: $m=4$, $\beta=10\,000\text{ s}^{-1}$ and $D=20\Delta x$ m. The maximum resolved frequency $f_{\max}=c/2\Delta x=2000$ Hz.

$$e^{-\sigma_y t} \frac{\partial e^{\sigma_y t} p_y}{\partial t} = -\rho_0 c^2 \frac{\partial v}{\partial y} - \nabla \cdot (u_0 p_y) - \frac{s(t) \delta(x|x_s)}{D},$$

$$e^{-\sigma_z t} \frac{\partial e^{\sigma_z t} p_z}{\partial t} = -\rho_0 c^2 \frac{\partial w}{\partial z} - \nabla \cdot (u_0 p_z) - \frac{s(t) \delta(x|x_s)}{D}. \quad (18)$$

Introduction of the PML in the extended Fourier PSTD method implies that the spatial derivative operator W of Eq. (15) now is constituted by all terms on the right side of Eqs. (18) apart from the source terms. The effect of the PML is imposed by an additional operator after every time step:

$$q'(x, t + \Delta t) = q'(x, t + \Delta t) e^{-\sigma' \Delta t}, \quad (19)$$

with $q' = [u, v, w, p_x, p_y, p_z]^T$ and $\sigma' = [\sigma_x, \sigma_y, \sigma_z, \sigma_x, \sigma_y, \sigma_z]^T$. The PML is theoretically reflection free for all angles under the condition that $\sigma_i(x)=0$ within a PML with the i -axis parallel to the outer domain boundary.⁹ Numerical artifacts from the PML can occur due the finite size of the PML i.e., reflection from the back of the PML and wrap-around effects inherent to the use of discrete Fourier transforms in a PS method and due to the discontinuity in damping at the interface of interior points and PML. Berenger therefore proposed to gradually increase the damping coefficients as for σ_x :

$$\sigma_x = \beta \left(\frac{x - x_{\text{PML}}}{D} \right)^m, \quad (20)$$

with $x - x_{\text{PML}}$ the position of the grid point in the PML layer, D the thickness of the layer, $x_{\text{PML}} \leq x \leq x_{\text{PML}} + D$, β the maximum amplitude of σ_x and m a real valued positive number. Numerical calculations have here been carried out to find suitable values for the constants β , D and m . Figure 3 shows the arithmetic averaged value of the reflection coefficient R_{PML} as a function of angle of incidence (0–80°, with 0 the normal to the interface) and frequency. The value of R_{PML} increases with frequency. The performance of the PML was found to improve with the thickness of the layer, except close to the maximum resolved frequency f_{\max} . The lower performance close to f_{\max} is likely due to the discontinuity of σ' at every discrete spatial step in the PML. This behavior has not been found in FDTD methods.⁹ The values used throughout in the presented calculations are $m=4$, and $\beta=10\,000\text{ s}^{-1}$ and $D=20\Delta x$ m. For receiver positions that are geometrically shadowed from the source, the performance of the PML

might be insufficient. For all calculations of the current paper, this was not the case.

III. TWO-DIMENSIONAL VALIDATION CALCULATIONS

A. Homogeneous non-moving atmosphere

The extended Fourier PSTD method is applied to four atmospheric acoustic applications for a non-moving medium. The geometries of the applications are related to community noise problems and a maximum frequency $f_{\max}=2000$ Hz has been chosen. The spatial Nyquist condition then requires a spatial discretization of $\Delta x = \Delta z = c/2f_{\max} = 0.085$ m. All dimensions printed in the figures are, in fact, multiples of Δx , but have been rounded. The domains are truncated at the open ends by the PML with coefficients given in Sec. II C. The time step was chosen to be $\Delta t = 1/(4f_{\max})$ s, since the RKo6s method is optimized up to four points per wavelength. This corresponds to a CFL number of $c\Delta t/\Delta x = 0.5$ and has led to stable schemes for all performed calculations.

In the implemented staggered equidistant grid, boundaries that form a horizontal interface have been chosen to coincide with pressure grid points and parallel velocity components. Boundaries that form a vertical interface have been chosen to coincide with the perpendicular velocity component nodes. The former has been chosen to easily model a source at a horizontal interface and the latter is numerically advantageous for a rigid thin screen.

1. Rigid thin screen

The first application is that of a rigid thin screen on a rigid ground surface. Figure 4(a) shows the modeled geometry and the location of the source and receivers. The source is positioned 6 m in front of the screen at zero height, which is a good approximation for the generation of tire-road noise. The screen is infinitesimally thin and 4 m tall, representing a commonly used noise screen along highways. The response is calculated at two receiver positions, at a height of 1.5 m above the ground surface and ranges 5 and 50 m behind the screen. From the computed time signals, only first order diffraction components and ground reflections are included and time signals have been tapered at both ends to prevent aliasing from high frequency components in the transformed domain. The calculated levels are plotted relative to the free field level. Results for the two receiver positions are compared with a ray method based on the 3-D diffraction model of Hadden and Pierce.^{38,39} The results of this model have been corrected in amplitude to obtain the 2-D solution (see e.g., Ref. 40). The results are shown in Figs. 4(b) and 4(c) and display an excellent agreement. The difference is hardly discernible except near f_{\max} .

2. Rigid thick screen

The second application is to a screen with a finite thickness of 1 m. Figure 4(d) shows the geometry of the problem. The source and receiver locations are the same as for the rigid thin screen case. Results from the calculations are again compared with a ray method, using the Hadden and Pierce

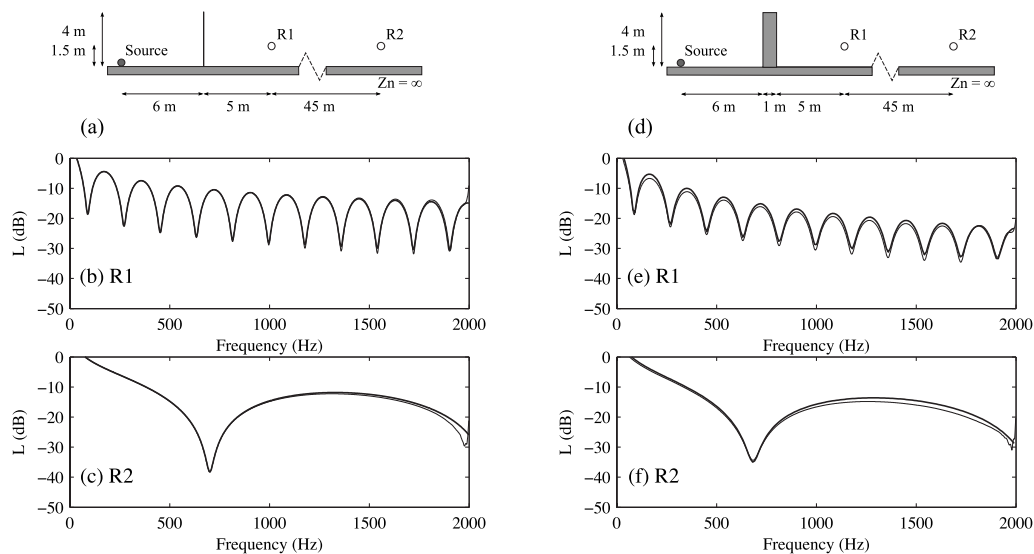


FIG. 4. Geometry with a rigid screen and related sound pressure levels. Levels are plotted relative to the free field level: (a) Thin screen; (d) 1 m thick screen; (b,e) Receiver position R1; (c,f) Receiver position R2. Solid thick: Reference calculations with the Hadden-Pierce method; Solid thin: Extended Fourier PSTD method results.

solution for the individual diffraction coefficients. The results clearly show a good agreement, although slightly less than for the thin screen.⁴¹

3. Double thin screens

A typical situation that can be encountered in the field of community noise is the geometry of a double rigid noise screen flanking a highway; see Fig. 5(a). In the modeling done here, the noise screens are thin and the ground surface is rigid. Figures 5(b) and 5(c) compare the extended Fourier PSTD results with results from a ray model. Up to 10 reflected rays have been included in both methods. To illustrate the importance of second order diffraction contributions as

included in the ray model, we isolate the first reflection from the left screen. Figure 5(d) shows the first 0.2 s of the calculated response at receiver position R1 where this first reflection is marked (between dashed lines). The following second order diffracted fields are included in the extended Fourier PSTD result of Fig. 5(e): left screen top-right screen top; right screen top-ground reflection-right screen top. The spectrum of the marked part is compared with the calculated spectrum using the ray model in Fig. 5(e). The ray model includes diffraction components either to first or second order. The extended Fourier PSTD results are in good agreement with the latter (almost indistinguishable except near f

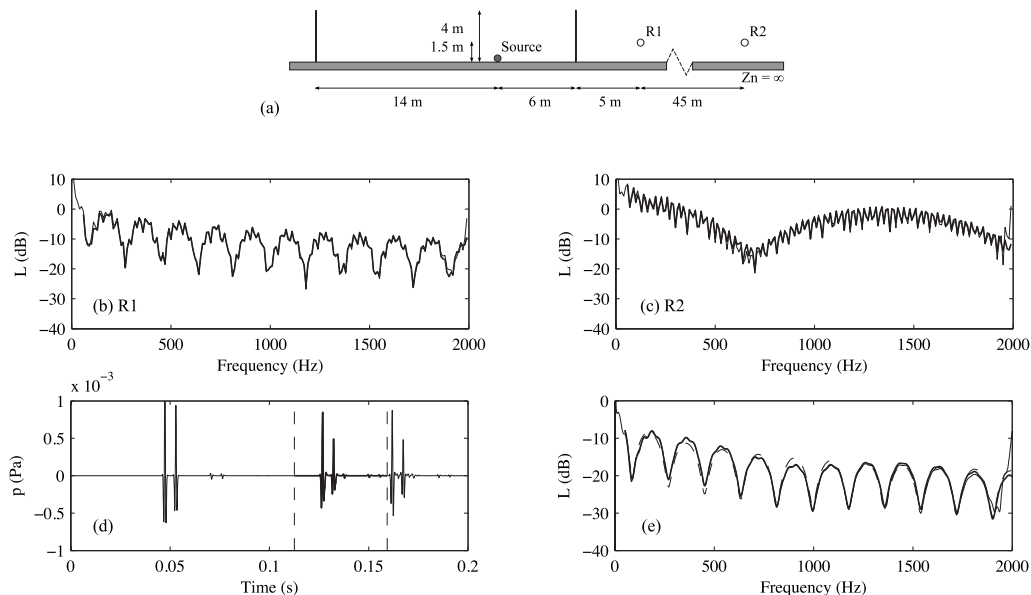


FIG. 5. Geometry with a double thin screen on a rigid ground surface and related sound pressure levels. Levels are plotted relative to the free field level. (a) Geometry; (b) 10 Hz-band results for receiver position R1; (c) 10 Hz-band results for receiver position R2. Solid thick: Reference calculations with a ray method; Solid thin: Extended Fourier PSTD method results. (d) First part of the extended Fourier PSTD calculated response at R1; (e) Calculated spectrum of first reflected component at R1. Solid thick: Ray method including 2nd order diffraction components; Dashed: Ray method including 1st order diffraction components; Solid thin: Extended Fourier PSTD result, i.e., the transformed solid thick part within dashed lines of (d).

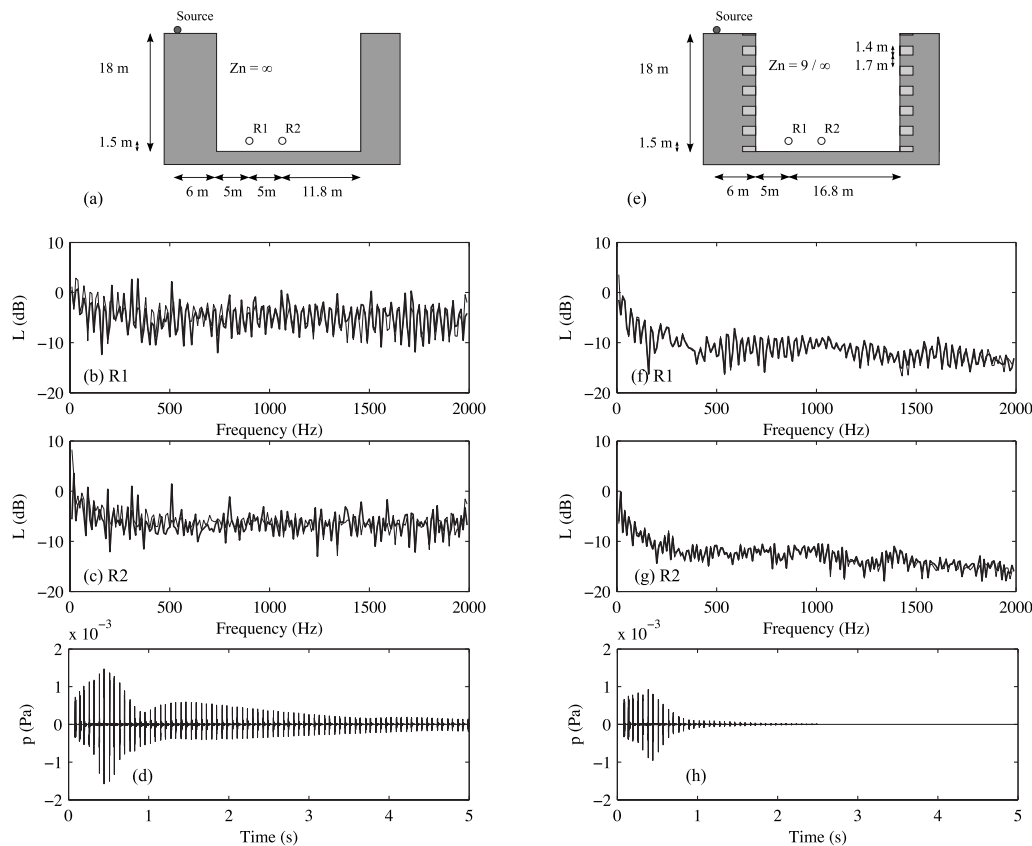


FIG. 6. Geometry with an urban canyon, related sound pressures and sound pressure levels. Levels are plotted relative to the free field level. (a) Rigid surfaces; (e) Façades with rigid and finite impedance parts ($Z_n=9$); (b, f) 10 Hz-band results for receiver position R1; (c, g) 10 Hz-band results for receiver position R2. Solid thick: Reference calculations with the ESM method; Solid thin: Extended Fourier PSTD method results. (d) Extended Fourier PSTD calculated response at R2 in canyon geometry (a); (h) Extended Fourier PSTD calculated response at R2 in canyon geometry (e).

$=f_{\max}$) and comparison with the first order diffraction ray method results clearly shows the importance of including second order diffraction components.

The spectrum including the 10 reflected rays is highly oscillating due to interference effects. For comparison, 10 Hz narrow band results are shown for R1 and R2 in Figs. 5(b) and 5(c). The agreement between the extended Fourier PSTD method and ray method is good, keeping the limitations of the ray method in mind.

4. Urban canyons

Of considerable interest in densely built-up urban environments is sound propagation into geometrically shielded areas such as courtyards.⁴² Fig. 6(a) shows a simplified geometry of a courtyard, here represented by a 2-D model, into which community noise is propagating over the urban roof level. The building blocks are 18 m high, corresponding to 6 story apartment buildings. At first, all boundaries are considered to be rigid. The levels relative to the free field level are calculated up to 40 000 time steps in the extended Fourier PSTD methods (corresponding to 5.0 s) and are compared to results from the equivalent sources method (ESM), a validated numerical method for this situation.⁴² The time response calculated at the receiver position R2 is shown in Fig. 6(d). The results over frequency are compared with the ESM results in Figs. 6(b) and 6(c), where the modes of the canyon dominate the 10 Hz-band levels. Both the phase and ampli-

tude of the two methods appear to be in good agreement. A second calculation has been done where the façades are modeled to have piecewise rigid and piecewise softer parts of the façade, with a finite normalized impedance of $Z_n=9$, see Fig. 6(e). Whereas this impedance is modeled by a second fluid with a different density in the extended Fourier PSTD method, it is a locally reacting boundary in the ESM method. Results are presented in Figs. 6(f) and 6(g) and show a very good agreement between both methods. A reasonable cause for the better agreement in the geometry of Fig. 6(e) is the shorter reverberation time compared with the hard façades case, where the 5 s impulse response from the extended Fourier PSTD has not died out completely, see Figs. 6(d) and 6(h).

B. Moving atmosphere

Atmospheric sound propagation is among others influenced by the state of the atmosphere. Due to the large difference in order of magnitude between the mean wind velocity and acoustic particle velocity, numerical reasons support to solve the flow and acoustic field separately.⁶ The acoustic field does not influence the flow, which is commonly assumed in atmospheric sound propagation, and the flow solution is used as input in the linearized Euler equations.

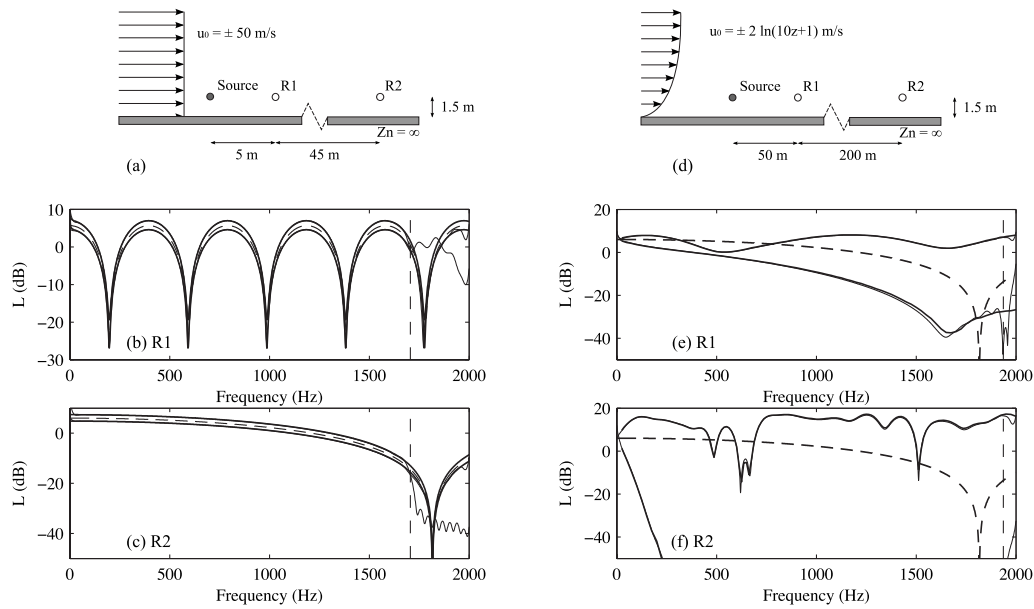


FIG. 7. Geometry with a rigid ground surface and related sound pressure levels. Levels are plotted relative to the free field level. (a) Geometry with uniform horizontal wind velocity; (d) Geometry with logarithmic horizontal wind velocity profile; (b,c) Upper curves for $u_0 = -50$ m/s and lower curves for $u_0 = 50$ m/s; (e, f) Upper curves for $u_0 = 2 \ln(10z+1)$ m/s and lower curves for $u_0 = -2 \ln(10z+1)$ m/s. Solid thick: Reference calculations with an analytical expression for case (a) and with the Fast Field Program for case (d); Solid thin: Extended Fourier PSTD method results. Dashed curves are the no-wind results. Vertical dashed lines correspond to the maximum resolved wave number for the upwind condition.

1. Horizontal wind velocity over rigid ground surface

Including moving medium components in the linearized Euler equations solved by the extended Fourier PSTD method is here first executed for a uniform horizontal wind velocity of $u_0 = \pm 50$ m/s (with slip ground surface conditions), as sketched in Fig. 7(a). These wind velocities are unrealistically high for meteorological conditions in the lower part of the atmosphere, but are used here as a test case. The results are compared in Fig. 7(b) and 7(c) with analytical results, which are valid for $k(|x_{\text{rec}} - x_s|) \gg 1$, see Ref. 7. The agreement is excellent for the larger part of the frequency region and the accuracy breaks down for the higher frequencies for the upwind condition, i.e., $u = -50$ m/s, as shown by the upper curves. The reason is that the highest wave number resolved by the spatial grid in the extended Fourier PSTD method corresponds to a lower frequency when the effective sound speed is lower. The number of points per wavelength thus needs to be increased. The corresponding maximum resolved frequency can be calculated by $f_s(c+u_0)/(2c)$ and is approximately 1706 Hz for $u_0 = -50$ m/s, indicated by the dashed vertical lines in Fig. 7(b) and 7(c). Since the stability criterion is related to the maximum sound speed, it is more strict for the $u_0 = 50$ m/s case, see e.g., Ref. 7. All here calculated cases were though found to be stable.

For a stable stratification in the atmosphere, a representative meteorological condition over a flat ground surface is the logarithmic wind velocity profile,

$$u_0(z) = b \log\left(\frac{z+z_0}{z_0}\right), \quad (21)$$

where the parameter z_0 is a roughness length for which 0.1 m has been used. The strength b is chosen to be either 2 or -2 m/s. These strengths correspond to strong down- and upward refraction, see e.g., Ref. 2. The results are compared with the

Fast Field Program (FFP) for receiver distances of 50 and 250 m. To make the extended Fourier PSTD calculation more efficient, a rightward moving grid has been introduced, limiting the necessary grid dimensions. For each time increment corresponding to one grid step per adiabatic sound speed c the spatial grid is moved one spatial grid step to the right, see Fig. 8. To account for the fact that the leftward traveling wave front leaves the left boundary of the domain with an additional relative horizontal velocity of $-c$, the vertical PML coefficients σ_z have been superposed with values of the horizontal components σ_x in the PML at the left boundary. Results are plotted in Figs. 7(e) and 7(f), along with the non-moving medium result. Results for an upward refracting condition, $b = -2$ m/s, display very low levels as the receiver points are located in a shadow zone. The comparison with FFP is good for the both receiver positions. The downward refracting case also shows strong wind effects and a good agreement between FFP and the extended Fourier PSTD method for both distances as well.

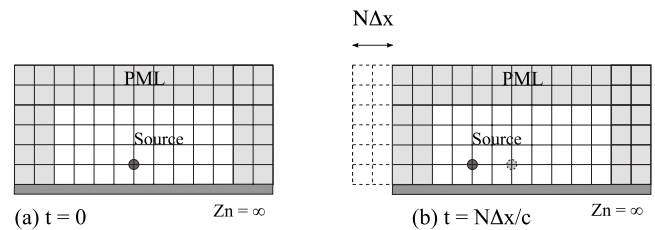


FIG. 8. Illustration of the moving-grid implementation for the extended Fourier PSTD calculation of Fig. 7(d). (a) Sketch of the numerical domain of sound propagation over a rigid ground surface; (b) At $t = N\Delta x/c$, the grid has been moved N discrete steps rightwards. Nodes left of the numerical domain drop off and nodes appearing at the right of the domain are zero valued. The source position moves along with the grid.

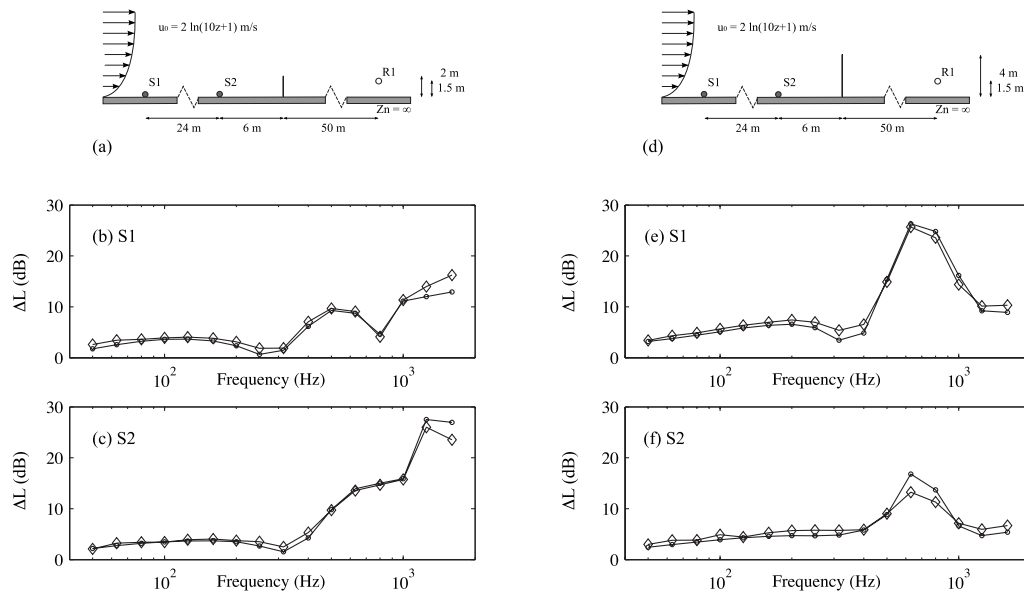


FIG. 9. Geometry with a rigid thin screen on a rigid ground surface in the presence of a downward refracting wind speed profile and 1/3-octave band levels relative to the levels without wind. (a) Screen height 2 m; (d) Screen height 4 m; (b, e) Results for source position S1; (c, f) Results for source position S2. Diamonds: PE method; Open circles: extended Fourier PSTD method.

2. Horizontal wind velocity and screen

A noise screen outdoors influences sound propagation directly (i.e., by reflection and diffraction) and indirectly by influencing the wind flow. The effect of meteorological conditions and the presence of a screen in the community noise context has been studied extensively.^{6,8–10,43–46} For sound propagation in the presence of a screen under downwind conditions, the screen induces a speed-up of the wind velocity profile just above the screen, which can reduce the performance of the screen.⁴⁷ Based on wind tunnel measurements and numerical calculations, Salomons and Rasmussen have proposed an analytical approximation for the mean wind field near a screen,⁴³ assuming an analytical wind velocity profile as in Eq. (21) well before the screen. It has been shown that the vertical component of the wind velocity has a small effect on the sound propagation and is neglected in this approximation.⁴⁴ Similarly, for a downwind situation in the presence of a screen, the effect of a realistic temperature gradient can be assumed to be negligible in comparison with the sharp wind velocity gradients.⁴⁴ For a 2 and 4 m tall, thin noise screen expressions for the screen induced wind velocity field associated with the undisturbed horizontal wind velocity profile of Eq. (21) and strength parameter $b = 2$ m/s were taken from Salomons and Rasmussen. The modeled source and receiver positions are found in Figs. 9(a) and 9(d). The results are compared with results obtained using the Crank-Nicholson PE method, which was also used by Salomons and Rasmussen.⁴³ Due to the Kirchhoff approximation this numerical method is only approximate in modeling sound propagation in the presence of a screen.⁴⁸ The implemented PE method further assumes an effective scalar sound speed. Using a vector wind implementation is not expected to alter the results significantly for the cases studied here. In shadowed receiver positions, PE results are known to fluctuate.⁴⁸ The PE results have therefore been averaged over 10 neighboring grid points (approximately correspond-

ing to one wavelength) and results are presented in 1/3-octave bands. Results are shown as levels in Fig. 9(b), 9(c), 9(e), and 9(f) relative to the no wind case and show a rather good agreement. The largest deviations between the methods are found for 1/3-octave bands where the no-wind case constitutes a destructive interference.

IV. THREE-DIMENSIONAL APPLICATION

To demonstrate the application of the extended Fourier PSTD in three dimensions, a 3-D example of sound propagation over a screen is made here. Figure 10(a) shows the geometry studied. The dark shaded part of the figure marks the footprint of the actual modeled part, with $\mathcal{N}_x \times \mathcal{N}_y \times \mathcal{N}_z = 256 \times 256 \times 128$ grid points. Since a PML has only been applied in the x - and z -direction, the results are affected by the periodicity in the y -direction. This means that responses from point sources at every $\mathcal{N}_y \Delta y$ m are received at the receiver locations. This distance has been chosen such that separate source contributions could be windowed from the time response and the screen effect could be found as a function of the y -distance between source and receiver.

A. Non-moving medium

Figure 10(b) shows the level relative to the free field level for a receiver positioned at $(x, y, z) = (30, 21.7, 1.5)$, from using the extended Fourier PSTD calculation and the 3-D Hadden and Pierce solution. The results show good agreement. In Fig. 10(c), the results are plotted as a function of the position along the y -axis for the 800 Hz 1/3-octave band, showing good agreement as well.

B. Horizontal wind velocity and screen

The wind velocity profile used in the 2-D calculations of Fig. 9 is now used in this 3-D geometry, invariant along the y -axis. Figure 10(d) shows the level relative to the no-wind

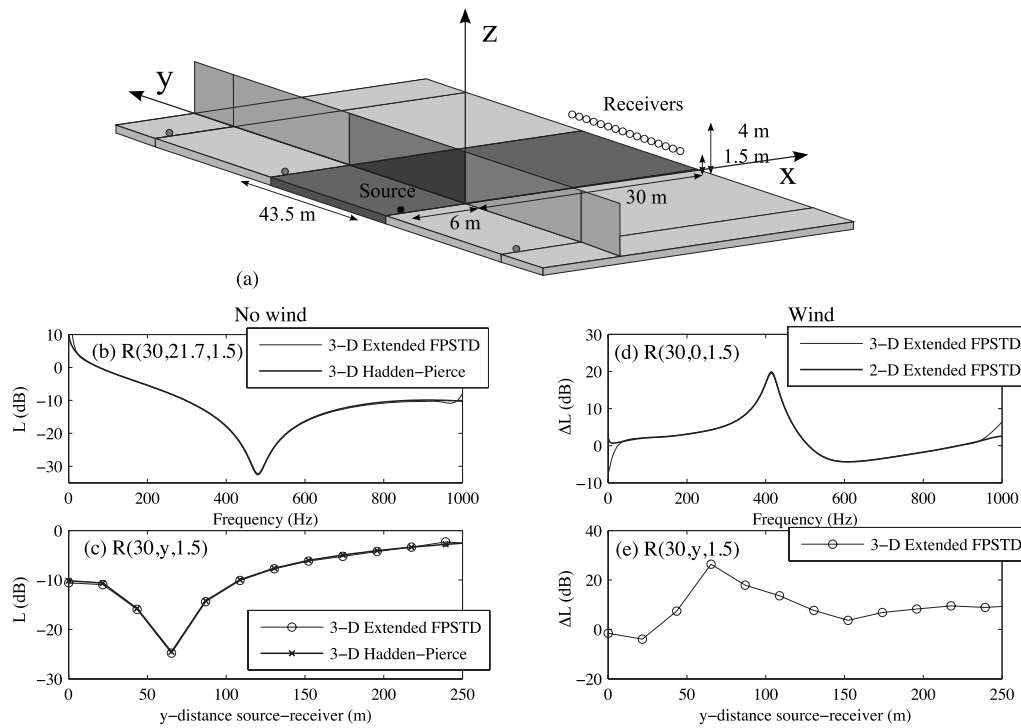


FIG. 10. Three-dimensional geometry with a rigid thin screen on a rigid ground surface and related sound pressure levels. (a) Geometry; (b,c) Levels relative to the free field level for the no-wind situation. (b) Receiver position (30,21.7,1.5); (c) Receiver position (30,y,1.5), 800 Hz 1/3-octave band result; (d,e) Results from the extended Fourier PSTD method with a horizontal wind velocity as from Fig. 9(d). Levels relative to the levels without wind. (d) Receiver position (30,0,1.5); (e) Receiver position (30,y,1.5), 800 Hz 1/3-octave band result.

result for receiver position (30,0,1.5) and is compared with the 2-D result from the extended Fourier PSTD method. Apart from discrepancy at low and high frequencies due to numerical artifacts, the insertion losses in 2-D and 3-D are very similar. Finally, ΔL from the 3-D calculation results is plotted for the 800 Hz 1/3-octave band as a function of the transverse source to receiver distance y .

V. COMPUTATIONAL COMPLEXITY

The computational efficiency of the Fourier PSTD method compared to a second-order accurate finite-difference method was reported on by Liu⁴⁹ among others. The computational costs for a single time step in the Fourier PSTD method amount to $\mathcal{K}_{\text{PS}} \mathcal{N}_{\text{PS}}^{\mathcal{D}} \log_2(\mathcal{N}_{\text{PS}})$. Here, the subscript PS denotes the pseudospectral method, \mathcal{D} is the dimensionality of the problem, \mathcal{K} a constant and \mathcal{N}_{PS} the discrete number of spatial points in one direction. The number of operations in the FDTD method can be estimated as $\mathcal{K}_{\text{FDTD}} (2\mathcal{N}_{\text{FDTD}})^{\mathcal{D}}$, where a single derivative operation costs two multiplications. For a similar accuracy, $\mathcal{N}_{\text{FDTD}}$ is a factor 4–8 larger than \mathcal{N}_{PS} . With these factors, the Fourier PSTD method was estimated to be $4^{\mathcal{D}} - 8^{\mathcal{D}}$ times as time-efficient as the FDTD method for $\mathcal{N}_{\text{PS}} = 64$.

Based on these results, we can make an estimate on the computational costs of the *extended* Fourier PSTD method for a 3-D situation with a low barrier as in Fig. 10(a). In the extended Fourier PSTD method, derivatives for a single medium amount to the same computational costs as the Fourier PSTD method, and take approximately 2 and 3 times as many operations for a derivative across 2 and 3 media respectively. For the barrier situation, the number of operations

in the extended Fourier PSTD method can therefore be estimated to be two times as large as in the Fourier PSTD method. Furthermore, the 3-D barrier problem with $\mathcal{N}_{\text{PS}} = 256$ requires more computational effort per grid point than from the reference case of Liu (as the operations for a single FFT scale with $\mathcal{N}_{\text{PS}} \log_2(\mathcal{N}_{\text{PS}})$). Taking these two factors into account, the computational efficiency factor of the extended Fourier PSTD over the FDTD method for the 3-D barrier situation can be estimated to be 24–192. Since the time steps in FDTD calculations are often smaller than in the extended Fourier PSTD method, an even larger factor will be obtained. Moreover, the storage capacity gain based on the number of grid points is $4^{\mathcal{D}} - 8^{\mathcal{D}}$.

VI. CONCLUSIONS

For 3-D atmospheric sound propagation problems with complex meteorology and topology, accurate time-domain solution methods to the linearized Euler equations, as the second-order-accurate finite-difference time-domain (FDTD) method, are demanding in calculation time and computational storage. Here, an extended Fourier pseudospectral time-domain (PSTD) method has been presented for these applications, which only requires two spatial points per wavelength and thereby reduces the computational storage and computation time as compared to the FDTD method. In comparison to the Fourier PSTD method, the extension refers to the ability to model media with discontinuous properties, while keeping the favorable computational efficiency and stability properties of the Fourier PSTD method. The extended Fourier PSTD method is able to solve the linear-

ized Euler equations for atmospheric sound propagation problems with complex meteorological conditions, ground surface and obstacles.

In the extended Fourier PSTD method, spatial derivatives are evaluated using the extended Fourier PS method, which is based on an eigenfunction expansion. The derivatives are evaluated in the wave number domain. Transforms to and from the wave number domain are executed by fast Fourier transforms. Time iteration in the method is done by a low-storage optimized 6-stage Runge-Kutta method.

Time-domain calculations are executed, with a perfectly matched layer (PML) at the non-reflecting boundaries. The derived extended Fourier PSTD method is validated for several 2-D geometries: sound propagation over a rigid ground surface in the presence of a thin rigid screen, a thick rigid screen and a double thin rigid screen, an urban canyon with rigid façades or piecewise finite impedance façade elements. In all cases, a coherent line source was modeled and results were evaluated up to two points per wavelength at receiver positions geometrically shielded from the source. Analytical and numerical methods were used for comparison. The thin screen, double screen and urban canyon cases with absorption showed excellent agreement up to two spatial points per wavelength. The latter case constitutes an example where modeling the boundary medium by a medium with a changed density is applicable. For the thick screen case, a small amplitude error was found, likely due to the discretization of the screen edges in the extended Fourier PSTD method. Further calculations were done for a horizontal wind velocity over a flat ground surface, either uniform or with a logarithmic profile. The latter in the absence and presence of a thin screen, including effects of the screen on background flow. Accurate results were obtained here as well.

Finally, a 3-D geometry example was considered. Sound propagation over a screen was modeled and gave accurate results. In the presence of wind, propagation downwind showed the dependence on the transverse source-receiver distance.

It can be concluded that the extended Fourier PSTD method presented here is accurate for many atmospheric sound propagation cases where meteorological and topological effects dominate. It provides a tool to calculate time-domain results with lower storage and calculation time than the standard FDTD method. A difficulty of the developed method is the treatment of two media. In this paper, the effect of planar boundaries have been modeled by an additional fluid with different density. Also, the performance of the non-reflecting boundaries is worst for the highest frequencies and could influence geometrically showed receiver positions. To solve problems with arbitrarily shaped boundary media with realistic properties, the Chebyshev PSTD method seems currently to be a better candidate.

ACKNOWLEDGMENTS

The work behind this paper was partly funded by the Swedish Foundation for Strategic Environmental Research (MISTRA) and by the European Commission under FP7-

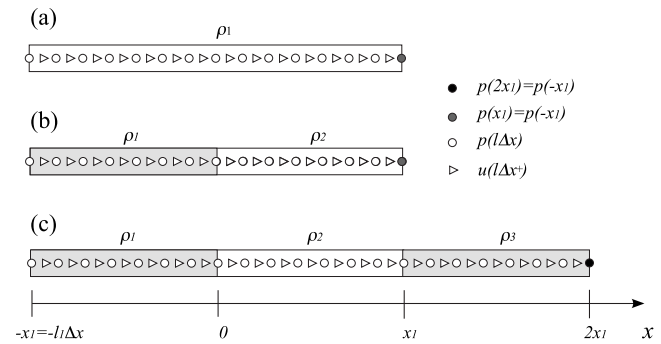


FIG. 11. Sketches of one-dimensional problems for: (a) A homogeneous fluid medium case with density ρ_1 ; (b) A two fluid media case with densities ρ_1 and ρ_2 ; (c) A three fluid media case with densities ρ_1 , ρ_2 and ρ_3 . Pressure and velocity grid points are staggered in space.

SST-2008-RTD-1, collaborative project HOSANNA, Project No. 234306.

APPENDIX

Spatial derivatives in the paper are calculated by the extended Fourier PS method developed in Sec. II. The spatial domain is discretized by an equidistant grid. To avoid spatial aliasing in a finite domain, the acoustic variables must have compact support within the spatial domain. To this end a PML has been implemented. The spatial derivatives that appear in the differential operator W of Eq. (15) may be evaluated separately on a 1-D basis. Figure 11 shows one-dimensional sketches for a single fluid medium, a two-media problem and a three-media problem. The media impedances differ only by their densities. Let $R_{i,i} = \rho_j c_j - \rho_i c_i / \rho_j c_j + \rho_i c_i$ and $T_{i,j} = 2\rho_j c_j / \rho_j c_j + \rho_i c_i$ be the physical reflection and transmission coefficients from medium i to medium i and j respectively.

For the cases of most interest in this paper, a single fluid and for a two-fluid case with a rigid second fluid, the derived expressions have been written in Eqs. (A1) and (A2). The general two-fluid derivatives are given by Eqs. (A3) and (A4). Some situations require derivatives across three media [as e.g., the horizontal derivative between two parallel walls in Fig. 6(e)]. An eigenfunction expansion for the three media case can be made similarly to the two media case. The corresponding coefficients to α_j, β_j in Eq. (10) will then contain exponentials which oscillate as a function of the wave number. Using the eigenfunctions to calculate the spatial derivatives will cause a periodically repeated solution in the spatial domain with the size of the bounded fluid as period length. Since the computational domain is finite, this is not desirable from a numerical point of view. Another approach is to use eigenfunctions that are an infinite summation of terms, analogous to multiple reflections, and truncate this summation. The latter approach is adopted here, with eigenfunctions and derivative expressions given by Eqs. (A5) and (A6). The relations to calculate spatial derivatives that are used in the paper thus are: derivatives for a single medium; derivatives for a single medium with one or two rigid boundaries; derivatives for two fluid media and derivatives for three fluid media. For all derivatives, transforms are evaluated using FFTs, imposing a two point per wavelength criterion on the

discrete spatial resolution of $q(x, t)$ and causing it to be periodic on the spatial domain. Details on the numerical implementation can be found elsewhere.⁵⁰

For a single medium, the expressions to calculate the spatial derivatives are given by

$$\begin{aligned} \left. \frac{\partial p}{\partial x} \right|_{l\Delta x^+} &= \mathcal{F}_x^{-1}(jk_x e^{-jk_x(\Delta x/2)} \mathcal{F}_x[p_1]), \quad -l_1 \leq l \leq l_1 - 1, \\ p_1 &= p(m\Delta x), \quad -l_1 \leq m \leq l_1 - 1, \\ \left. \frac{\partial u}{\partial x} \right|_{l\Delta x} &= \mathcal{F}_x^{-1}(jk_x e^{jk_x(\Delta x/2)} \mathcal{F}_x[u_1]), \quad -l_1 \leq l \leq l_1 - 1, \\ u_1 &= u(m\Delta x^+), \quad -l_1 \leq m \leq l_1 - 1, \end{aligned} \quad (\text{A1})$$

where Δx^+ denotes $\Delta x + (\Delta x/2)$, k_x the wave number in the x -direction, \mathcal{F}_x is the forward and \mathcal{F}_x^{-1} the inverse Fourier transform over and to the x -variable and $x \in [-x_1, x_1]$ as in Fig. 11(a). As discussed in Sec. II A, a grid with pressure and velocity components staggered in space is used. To evaluate derivatives at positions staggered by $\mp \Delta x/2$, spatial derivatives in Eq. (A1) are multiplied in the wave number domain by $e^{\pm jk_x(\Delta x/2)}$. Derivatives to be evaluated at non-staggered positions are obtained by omitting these terms. Note that Eq. (A1) is a discrete version of Eq. (2). For a derivative along a direction with a rigid termination at $x=0$ we find

$$\begin{aligned} \left. \frac{\partial p}{\partial x} \right|_{l\Delta x^+} &= \mathcal{F}_x^{-1}(jk_x e^{-jk_x(\Delta x/2)} \mathcal{F}_x[p_2]), \quad 0 \leq l \leq l_1 - 1, \\ p_2 &= p(|m\Delta x|), \quad -l_1 \leq m \leq l_1 - 1, \\ \left. \frac{\partial u}{\partial x} \right|_{l\Delta x} &= \mathcal{F}_x^{-1}(jk_x e^{jk_x(\Delta x/2)} \mathcal{F}_x[u_2]), \quad 0 \leq l \leq l_1, \end{aligned}$$

$$u_2 = \text{sgn}(m)u(|m\Delta x^+|), \quad -l_1 \leq m \leq l_1 - 1, \quad (\text{A2})$$

with $\text{sgn}(x)$ the signum function. Note that this is a discrete version of Eq. (3).

For the two-media case of Fig. 11(b) where the second medium has a different density as of Fig. 11(b), the derivatives are as follows:

$$\begin{aligned} \left. \frac{\partial p}{\partial x} \right|_{l\Delta x^+} &= \mathcal{F}_x^{-1}\left(jk_x e^{-jk_x(\Delta x/2)} \mathcal{F}_x \begin{bmatrix} p_1 \\ p_2 \end{bmatrix}\right), \quad \begin{aligned} -l_1 \leq l \leq -1, \\ 0 \leq l \leq l_1 - 1, \end{aligned} \\ p_1 &= \begin{cases} p(m\Delta x), & -l_1 \leq m \leq -1 \\ R_{1,1}p(-m\Delta x) + T_{2,1}p(m\Delta x), & 0 \leq m \leq l_1 - 1, \end{cases} \\ p_2 &= \begin{cases} R_{2,2}p(-m\Delta x) + T_{1,2}p(m\Delta x), & -l_1 \leq m \leq -1 \\ p(m\Delta x), & 0 \leq m \leq l_1 - 1, \end{cases} \end{aligned} \quad (\text{A3})$$

$$\begin{aligned} \left. \frac{\partial u}{\partial x} \right|_{l\Delta x} &= \mathcal{F}_x^{-1}\left(jk_x e^{jk_x(\Delta x/2)} \mathcal{F}_x \begin{bmatrix} u_1 \\ u_2 \end{bmatrix}\right), \quad \begin{aligned} -l_1 \leq l \leq -1, \\ 0 \leq l \leq l_1 - 1, \end{aligned} \\ u_1 &= \begin{cases} u(m\Delta x^+), & -l_1 \leq m \leq -1 \\ -R_{1,1}u(-m\Delta x^+) + T_{1,2}u(m\Delta x^+), & 0 \leq m \leq l_1 - 1, \end{cases} \\ u_2 &= \begin{cases} -R_{2,2}u(-m\Delta x^+) + T_{2,1}u(m\Delta x^+), & -l_1 \leq m \leq -1 \\ u(m\Delta x^+), & 0 \leq m \leq l_1 - 1. \end{cases} \end{aligned} \quad (\text{A4})$$

For a rigid medium 1, one has $R_{2,2}=1$ and it reduces to Eq. (A2).

For the three-media case of Fig. 11(c), the derivatives have been calculated based on the following eigenfunctions for three media:

$$\psi_-(k_x, x) = N_-(k_x).$$

$$\begin{cases} \begin{bmatrix} -\frac{1}{\rho_1 c} \left(\alpha_{1,0}^- e^{-jk_x x} - e^{jk_x x} \sum_{n=0}^{\infty} \beta_{1,n}^- e^{-jk_x(2n)x_1} \right) \\ \alpha_{1,0}^- e^{-jk_x x} + e^{jk_x x} \sum_{n=0}^{\infty} \beta_{1,n}^- e^{-jk_x(2n)x_1} \end{bmatrix}, & -x_1 \leq x \leq 0 \\ \begin{bmatrix} -\frac{1}{\rho_2 c} \left(\alpha_{2,0}^- e^{-jk_x x} - e^{jk_x x} \left(\sum_{n=1}^{\infty} \beta_{2,n}^- e^{-jk_x(2n)x_1} - \sum_{m=1}^{\infty} \alpha_{2,m}^- e^{-jk_x((2m)x_1+2x)} \right) \right) \\ \alpha_{2,0}^- e^{-jk_x x} + e^{jk_x x} \left(\sum_{n=1}^{\infty} \beta_{2,n}^- e^{-jk_x(2n)x_1} + \sum_{m=1}^{\infty} \alpha_{2,m}^- e^{-jk_x((2m)x_1+2x)} \right) \end{bmatrix}, & 0 \leq x \leq x_1 \\ \begin{bmatrix} -\frac{1}{\rho_3 c} e^{-jk_x x} \\ e^{-jk_x x} \end{bmatrix}, & x_1 \leq x \leq x_3, \end{cases}$$

$$\psi_+(k_x, x) = N_+(k_x) \cdot \begin{cases} \begin{bmatrix} \frac{1}{\rho_1 c} e^{jk_x x} \\ e^{jk_x x} \end{bmatrix}, & -x_1 \leq x \leq 0 \\ \frac{1}{\rho_2 c} \left(\alpha_{2,0}^+ e^{jk_x x} - e^{-jk_x x} \left(\sum_{n=1}^{\infty} \beta_{2,n}^+ e^{jk_x(2n)x_1} - \sum_{m=1}^{\infty} \alpha_{2,m}^+ e^{jk_x((2m)x_1+2x)} \right) \right) \\ \alpha_{2,0}^+ e^{jk_x x} + e^{-jk_x x} \left(\sum_{n=1}^{\infty} \beta_{2,n}^+ e^{jk_x(2n)x_1} + \sum_{m=1}^{\infty} \alpha_{2,m}^+ e^{jk_x((2m)x_1+2x)} \right) \end{bmatrix}, & 0 \leq x \leq x_1 \\ \begin{bmatrix} \frac{1}{\rho_3 c} \left(\alpha_{3,0}^+ e^{jk_x x} - e^{-jk_x x} \sum_{n=0}^{\infty} \beta_{3,n}^+ e^{jk_x(2n)x_1} \right) \\ \alpha_{3,0}^+ e^{jk_x x} + e^{-jk_x x} \sum_{n=0}^{\infty} \beta_{3,n}^+ e^{jk_x(2n)x_1} \end{bmatrix}, & x_1 \leq x \leq 2x_1, \end{cases} \quad (\text{A5})$$

where the coefficients α and β are indexed by subscripts respectively denoting the medium and the reflection order and where the superscript denotes the corresponding eigenfunction. From the eigenfunctions, only the expressions up to $n, m=0$ are used in the calculation of the derivatives, i.e., a zero order approach. This approach corresponds to a superposition of two two-fluid problems, and will be a good approximation if the Gibbs phenomena occurring at the two discontinuities do not influence each other. This means that the number of discrete points between the discontinuities needs to be sufficiently large for the oscillations (which characterize Gibbs phenomenon) to die out, e.g., 32 points, see Ref. 18. This approach has been found to be sufficient for the applications in the paper. The derivatives of the pressure and velocity are now calculated as:

$$\begin{aligned} \left. \frac{\partial p}{\partial x} \right|_{l\Delta x^+} &= \mathcal{F}_x^{-1} \left(jk_x e^{-jk_x(\Delta x/2)} \mathcal{F}_x \begin{bmatrix} p_1 \\ p_2 \\ p_3 \end{bmatrix} \right), \quad \begin{aligned} &-l_1 \leq l \leq -1, \\ &0 \leq l \leq l_1 - 1, \\ &l_1 \leq l \leq 2l_1 - 1, \end{aligned} \\ p_1 &= \begin{cases} p(m\Delta x), & -l_1 \leq m \leq -1 \\ R_{1,1}p(-m\Delta x) + T_{2,1}p(m\Delta x), & 0 \leq m \leq l_1 - 1, \end{cases} \\ p_2 &= \begin{cases} R_{2,2}p(-m\Delta x) + T_{1,2}p(m\Delta x), & -l_1 \leq m \leq -1 \\ p(m\Delta x), & 0 \leq m \leq l_1 - 1 \\ R_{2,2}p(2x_1 - m\Delta x) + T_{3,2}p(m\Delta x), & l_1 \leq m \leq 2l_1 - 1, \end{cases} \\ p_3 &= \begin{cases} R_{3,3}p(2x_1 - m\Delta x) + T_{2,3}p(m\Delta x), & 0 \leq m \leq l_1 - 1 \\ p(m\Delta x), & l_1 \leq m \leq 2l_1 - 1, \end{cases} \end{aligned} \quad (\text{A6})$$

$$\begin{aligned} \left. \frac{\partial u}{\partial x} \right|_{l\Delta x} &= \mathcal{F}_x^{-1} \left(jk_x e^{jk_x(\Delta x/2)} \mathcal{F}_x \begin{bmatrix} u_1 \\ u_2 \\ u_3 \end{bmatrix} \right), \quad \begin{aligned} &-l_1 \leq l \leq -1, \\ &0 \leq l \leq l_1 - 1, \\ &l_1 \leq l \leq 2l_1 - 1, \end{aligned} \\ u_1 &= \begin{cases} u(m\Delta x^+), & -l_1 \leq m \leq -1 \\ -R_{1,1}u(-m\Delta x^+) + T_{1,2}u(m\Delta x^+), & 0 \leq m \leq l_1 - 1, \end{cases} \\ u_2 &= \begin{cases} -R_{2,2}u(-m\Delta x^+) + T_{2,1}u(m\Delta x^+), & -l_1 \leq m \leq -1 \\ u(m\Delta x^+), & 0 \leq m \leq l_1 - 1 \\ -R_{2,2}u(2x_1 - m\Delta x^+) + T_{2,3}u(m\Delta x^+), & l_1 \leq m \leq 2l_1 - 1, \end{cases} \\ u_3 &= \begin{cases} -R_{3,3}u(2x_1 - m\Delta x^+) + T_{3,2}u(m\Delta x^+), & 0 \leq m \leq l_1 - 1 \\ u(m\Delta x^+), & l_1 \leq m \leq 2l_1 - 1. \end{cases} \end{aligned} \quad (\text{A7})$$

When both medium 1 and 3 are rigid, Eqs. (A2) apply.

- ¹B. Plovsing and J. Kragh, "Nord2000. Comprehensive outdoor sound propagation model. Part 2: Propagation in an atmosphere with refraction," Report No. AV 1851/00, Delta Acoustics & Vibration, Lyngby, Denmark, 2001.
- ²J. Defrance, E. Salomons, I. Noordhoek, D. Heimann, B. Plovsing, G. Watts, H. Jonasson, X. Zhang, E. Premat, I. Schmich, F. Aballea, M. Baulac, and F. de Roo, "Outdoor sound propagation reference model developed in the European harmonoise project," *Acust. Acta Acust.* **93**, 213–227 (2007).
- ³E. M. Salomons, *Computational Atmospheric Acoustics* (Kluwer, Dordrecht, 2001), p. 153 and 163–164.
- ⁴E. Premat and Y. Gabillet, "A new boundary-element method for predicting outdoor sound propagation and application to the case of a sound barrier in the presence of downward refraction," *J. Acoust. Soc. Am.* **108**, 2775–2783 (2000).
- ⁵E. M. Salomons, R. Blumrich, and D. Heimann, "Eulerian time-domain model for sound propagation over a finite-impedance ground surface. Comparison with frequency-domain models," *Acust. Acta Acust.* **88**, 483–492 (2002).
- ⁶R. Blumrich and D. Heimann, "A linearized Eulerian sound propagation model for studies of complex meteorological effects," *J. Acoust. Soc. Am.* **112**, 446–455 (2002).
- ⁷V. E. Ostashev, D. K. Wilson, L. Liu, D. F. Aldridge, N. P. Symons, and D. Marlin, "Equations for finite-difference, time-domain simulation of sound

- propagation in moving inhomogeneous media and numerical implementation," J. Acoust. Soc. Am. **117**, 503–517 (2005).
- ⁸D. Heimann and R. Blumrich, "Time-domain simulations of sound propagation through screen-induced turbulence," Appl. Acoust. **65**, 561–582 (2004).
- ⁹T. Van Renterghem, "The finite-difference time-domain method for simulation of sound propagation in a moving medium," Ph.D. thesis, Ghent University, Ghent, Belgium (2003).
- ¹⁰D. Heimann, "Three-dimensional linearised Euler model simulations of sound propagation in idealised urban situations with wind effects," Appl. Acoust. **68**, 217–237 (2007).
- ¹¹D. Albert, L. Liu, and M. L. Moran, "Time reversal processing for source location in an urban environment," J. Acoust. Soc. Am. **118**, 616–619 (2005).
- ¹²U. Kristiansen and K. Jezzine, "TLM model for sound propagation above ground," in Proceedings of the Internoise, Nice, France (2000).
- ¹³J. Hofmann and K. Heutschi, "Simulation of outdoor sound propagation with a transmission line matrix method," Appl. Acoust. **68**, 158–172 (2007).
- ¹⁴G. Guillaume, J. Picaut and G. Dutilleul, "Use of the transmission line matrix method for the sound propagation modelling in urban area," in Proceedings of the Acoustics '08, Paris, France (2008).
- ¹⁵C. K. W. Tam and J. C. Webb, "Dispersion-relation-preserving finite difference schemes for computational acoustics," J. Comput. Phys. **107**, 262–281 (1993).
- ¹⁶C. Bogey and C. Bailly, "A family of low dispersive and low dissipative explicit schemes for flow and noise computation," J. Comput. Phys. **194**, 194–214 (2004).
- ¹⁷D. Mast, L. Souriau, D.-L. Liu, M. Tabei, A. Nachman, and R. Waag, "A k -space method for large-scale models of wave propagation in tissue," IEEE Trans. Ultrason. Ferroelectr. Freq. Control **48**, 341–354 (2001).
- ¹⁸J. Hesthaven, S. Gottlieb and D. Gottlieb, in *Spectral Methods for Time-Dependent Problems*, Cambridge Monographs on Applied and Computational Mathematics (Cambridge University Press, Cambridge, 2007), p. 17, 190, and 153–186.
- ¹⁹G.-X. Fan, Q. H. Liu, and J. S. Hesthaven, "Multidomain pseudospectral time-domain simulations of scattering by objects buried in lossy media," IEEE Trans. Geosci. Remote Sens. **40**, 1366–1373 (2002).
- ²⁰X. Huang and X. Zhang, "A Fourier pseudospectral method for some computational aeroacoustics problems," Int. J. Aeroacoust. **5**, 279–294 (2006).
- ²¹B. Cox, S. Kara, S. Arridge, and P. Beard, " k -space propagation models for acoustically heterogeneous media: Application to biomedical photoacoustics," J. Acoust. Soc. Am. **121**, 3453–3464 (2007).
- ²²B. Fornberg, "The pseudospectral method: Comparisons with finite differences for the elastic wave equation," Geophysics **52**, 483–501 (1987).
- ²³C. E. Wasberg and Ø. Andreassen, "Pseudospectral methods with open boundary conditions for the study of atmospheric wave phenomena," Comput. Methods Appl. Mech. Eng. **80**, 459–465 (1990).
- ²⁴Ø. Andreassen and I. Lie, "Simulation of acoustical and elastic waves and their interaction," J. Acoust. Soc. Am. **95**, 171–186 (1994).
- ²⁵M. Hornikx and R. Waxler, "An eigenfunction expansion method to efficiently evaluate spatial derivatives for media with discontinuous properties," in Proceedings of the Acoustics '08 Conference, Paris, France (2008).
- ²⁶M. Hornikx and R. Waxler, "The extended pseudospectral Time-Domain (PSTD) method for fluid media with discontinuous properties," J. Comput. Acoust. In press (2010).
- ²⁷L. Råde and B. Westergren, *Mathematics Handbook for Science and Engineering* (Studentlitteratur, Lund, Sweden, 2004), pp. 261–262.
- ²⁸T. Özdenvar and G. A. McMechan, "Causes and reduction of numerical artefacts in pseudo-spectral wavefield extrapolation," Geophys. J. Int. **126**, 819–828 (1996).
- ²⁹H. W. Chen, "Staggered-grid pseudospectral viscoacoustic wave field simulation in two-dimensional media," J. Acoust. Soc. Am. **100**, 120–131 (1996).
- ³⁰D. Stanescu and W. G. Habashi, "2N-storage low dissipation and dispersion Runge-Kutta schemes for computational acoustics," J. Comput. Phys. **143**, 674–681 (1998).
- ³¹M.H. Carpenter and C.A. Kennedy, "A fourth-order 2N storage Runge-Kutta scheme," Report No. TM-109112, NASA, Washington, DC, 1994.
- ³²J. P. Berenger, "A perfectly matched layer for the absorption of electromagnetic waves," J. Comput. Phys. **114**, 185–200 (1994).
- ³³F. Q. Hu, "On absorbing boundary conditions for linearized Euler equations by a perfectly matched layer," J. Comput. Phys. **129**, 201–219 (1996).
- ³⁴M. Tabei, T. Mast, and R. Waag, "A k -space method for coupled first-order acoustic propagation equations," J. Acoust. Soc. Am. **111**, 53–63 (2002).
- ³⁵G. X. Fan and Q. H. Liu, "A well-posed PML absorbing boundary condition for lossy media," IEEE Antennas Propagat. Soc. Int. Sym. **3**, 2–5 (2001).
- ³⁶J. A. Roden and S. D. Gedney, "Convolution PML (CPML): An efficient FDTD implementation of the CFS-PML for arbitrary media," Microwave Opt. Technol. Lett. **27**, 334–339 (2000).
- ³⁷X. Yuan, D. Borup, J. Wiskin, M. Berggren, and S. A. Johnson, "Simulation of acoustic wave propagation in dispersive media with relaxation losses by using FDTD method with PML absorbing boundary condition," IEEE Trans. Ultrason. Ferroelectr. Freq. Control **46**, 14–23 (1999).
- ³⁸J. W. Hadden and A. D. Pierce, "Erratum: Sound diffraction around screens and wedges for arbitrary point source locations," J. Acoust. Soc. Am. **71**, 1290 (1982).
- ³⁹E. M. Salomons, "Sound propagation in complex outdoor situations with a non-refracting atmosphere: Model based on analytical solutions for diffraction and reflection," Acust. Acta Acust. **83**, 436–454 (1997).
- ⁴⁰T. Van Renterghem, E. Salomons, and D. Botteldooren, "Efficient FDTD-PE model for sound propagation in situations with complex obstacles and wind profiles," Acust. Acta Acust. **91**, 671–679 (2005).
- ⁴¹One reason is that the Hadden and Pierce solution is valid for screen widths much larger than a wavelength. Calculation for a 10 m wide screen (not plotted here) indeed showed a better agreement for the lower frequencies. As with the 1 m wide screen, a disagreement is still present for the higher frequencies. This can be attributed to the discretization of a corner in the implemented extended Fourier PSTD method; media interfaces are allocated explicitly whereas corners are not.
- ⁴²M. Ögren, "Prediction of traffic noise shielding by city canyons," Ph.D. thesis, Chalmers University of Technology, Gothenburg, Sweden (2004).
- ⁴³E. M. Salomons and K. B. Rasmussen, "Numerical computation of sound propagation over a noise screen based on an analytic approximation of the wind speed field," Appl. Acoust. **60**, 327–341 (2000).
- ⁴⁴R. Blumrich and D. Heimann, "Numerical estimation of atmospheric approximation effects in outdoor sound propagation modelling," Acust. Acta Acust. **90**, 24–37 (2004).
- ⁴⁵L. B. Rolla and H. J. Rice, "A forward-advancing wave expansion method for numerical solution of large-scale sound propagation problems," J. Sound Vib. **296**, 406–415 (2006).
- ⁴⁶T. Van Renterghem and D. Botteldooren, "Numerical evaluation of tree canopy shape near noise barriers to improve downwind shielding," J. Acoust. Soc. Am. **123**, 648–657 (2008).
- ⁴⁷E. M. Salomons, "Reduction of the performance of a noise screen due to screen-induced wind-speed gradients. Numerical computations and wind-tunnel experiments," J. Acoust. Soc. Am. **105**, 2287–2293 (1999).
- ⁴⁸E. M. Salomons, "Diffraction by a screen in downwind sound propagation: A parabolic-equation approach," J. Acoust. Soc. Am. **95**, 3109–3117 (1994).
- ⁴⁹Q. Liu, "The PSTD algorithm: A time-domain method requiring only two cells per wavelength," Microwave Opt. Technol. Lett. **15**, 158–165 (1997).
- ⁵⁰M. Hornikx, "Numerical modelling of sound propagation to closed urban courtyards," Ph.D. thesis, Chalmers University of Technology, Gothenburg, Sweden (2009).